Collision dynamics of nanoscale Lennard-Jones clusters

Marco Kalweit* and Dimitris Drikakis†
Aerospace Sciences Department, Fluid Mechanics and Computational Science Group, Cranfield University, Cranfield, Bedfordshire MK43 0AL, United Kingdom

(Received 10 June 2006; revised manuscript received 19 September 2006; published 11 December 2006)

An investigation of collision dynamics of nanoparticles for a broad range of impact factors and collision speeds is presented. The investigation is based on molecular dynamics simulations in conjunction with the Lennard-Jones interaction potential thus making the results applicable for a broad range of material properties. Identification criteria are used to classify the collision dynamics into different collision modes and submodes. Detailed analysis of the collision processes reveals the existence of coalescence and stretching separation modes, which are further classified according to their dynamics into sticking; slide-and-locking; droplet; normal stretching separation; stretching separation with satellite droplets; and shearing-off modes. Qualitative and quantitative comparisons with previous molecular dynamic studies and analytical prediction models derived for macroscopic droplet collisions are also discussed. The investigation reveals that the reflexive separation mode, which has been observed in macroscopic droplet collisions, does not occur for nanoparticles consisting of 10 000 (or less) atoms.

DOI: 10.1103/PhysRevB.74.235415 PACS number(s): 82.30.Nr

I. INTRODUCTION

The interaction of particles, i.e., drops, droplets or clusters, plays an important role in various natural phenomena and technical applications. Understanding of collision dynamics of binary droplets under different conditions is pertinent to a broad range of processes including nucleation and growth of aerosols in the atmosphere;[1,2] technical sprays used in material manufacturing processes, internal combustion engines, surface treatment and coating;[2–4] sintering during which bulk material is generated through interparticle collisions, where the properties of the material depend strongly on the shape of the coalescence or agglomerated particles;[5,6] and growth, handling and utilization of atomic and molecular clusters,[7] particularly as applied in cluster beams, where the growth of clusters is driven by monomer addition and cluster coalescence.[8] Furthermore, research studies have been conducted to understand the fundamental mechanisms associated with coalescence of liquid drops[9] as well as drop deformation and breakup in viscous flows.[10]

Binary collisions of particles can occur at different scales ranging from macroscopic particles, such as raindrops, down to nanosized particles, i.e., clusters and nanodroplets. In the context of macroscopic scales, binary collisions of droplets have been the subject of extensive investigations over the last few decades. Experimental studies of Ashgriz and Poo,[1] Qian and Law,[2] Brazier-Smith *et al.*,[11] Brenn *et al.*,[12] and Willis and Orme[13,14] have identified four main collision modes: coalescence, reflexive separation, stretching separation, and shattering. Models predicting the outcome of a collision for a given set of initial conditions have been developed and enhanced using experimental results, e.g., Ashgriz and Poo,[1] Post and Abraham,[3] Ko and Ryou,[4] Brazier-Smith *et al.*,[11] Arkhipov *et al.*,[15] and Gopinath and Koch.[16] However, the details of the collision processes are difficult to be obtained through experiments, especially at small length and time scales.

As an alternative, numerical simulations can be employed to shed light into the details of collisions. Previous studies on three-dimensional simulations of binary droplet collisions have been presented by Rieber and Frohn,[17] based on the incompressible Navier-Stokes equations in conjunction with the volume-of-fluid method, and Schelke and Frohn[18] based on the lattice Boltzmann equation method. Mashayek *et al.*[19] used the Galerkin finite element method to simulate the coalescence of liquid droplets in two dimensions. The method is limited to coalescence and cannot handle separation. Meleán and Sigalotti[20] employed smoothed particle hydrodynamics (SPH) to simulate the binary collisions of equal-sized drops in two dimensions, while simulations based on the incompressible Navier-Stokes equations covering main modes of binary droplet collisions have also been recently presented by Pan and Suga.[21]

At nanoscale, the atomic structure of the particles becomes important since they consist of a few hundred or thousand of atoms. At present, these scales are not directly accessible by experiments, hence, numerical simulations become even more important. Quantum mechanical methods such as the density functional theory (DFT) would give the most accurate results, but they are computationally very expensive and can only be applied to small clusters. Molecular dynamics (MD) methods based on phenomenological potential functions to model interatomic interactions have turned out to be an excellent tool for conducting numerical experiments at small scales. Continuum methods would reduce the computational effort even further, but they are not valid in the nanoscale range.

Greenspan[22] and Greenspan and Heath[23] presented two-dimensional (2D) and three-dimensional (3D) molecular dynamics simulations of droplets consisting of 1128 molecules interacting via a Lennard-Jones potential. The simulations showed that coalescence, stretching separation, and shattering modes occur for droplet collisions at nanoscale. Wyatt[24] presented results from MD simulations of binary collisions of $(H_2O)_{400}$ droplets using the simple point charge model (SPC) and a newly derived hybrid model (HYB) for the water molecules. The first systematic investigations of binary

collisions were performed by Ming *et al.*[25] for Ar_{1000} clusters, for different collision velocities and angles, confirming the modes found in previous studies, i.e., coalescence, stretching separation, and shattering. Svanberg *et al.*[26] employed the same setup for the simulation of $(H_2O)_{125}$ and $(H_2O)_{1000}$ and performed simulations for two different initial temperatures of 160 K and 300 K in conjunction with the SPC water model. They found that the boundary between coalescence and stretching separation is in good agreement with macroscopic models. However, reflexive separation which is observed at macroscale was not found in any of the above investigations. In a previous study, the authors have investigated the collision dynamics of the head-on impact of a small cluster (Ar_{309}) onto a large cluster (Ar_{10973}) for a broad range of impact speeds.[27] Both clusters had an initial temperature of 5 K. In addition to coalescence, the collisions resulted in partial scattering, eversion, and total disintegration (shattering).

For sintering, collisions between clusters at thermal energies, i.e., at very low speeds, which are likely to lead to the coalescence of the involved particles, play a key role at nanoscale level. MD simulations of these processes are performed by starting with two equilibrated clusters, initially placed in single point contact with each other. As the simulation advances, the attracting interatomic forces cause the coalescence of the two clusters, which takes place through two distinguishable stages: Initially a neck, following a power-law growth, forms between the clusters. The neck disappears later and one particle is formed. Several authors have compared MD results with phenomenological models for coalescence time, neck growth, surface area reduction, temperature change, and change of gyration radii. Simulations for coalescence of Si_{15} clusters were carried out by Blaisten-Barojas and Zachariah.[28] A combination of MD and DFT was used by Schmidt *et al.*[29] to study the fusion and reaction cross sections of small metal-metal cluster collisions. Zachariah and Carrier[6] performed MD simulations to investigate the morphology of particles in binary collisions of spherical silicon particles, created by coalescence of zero impact factor (see Sec. IV for definition), and validate phenomenological models of particle growth. They found that the shape of the generated particles (from 30 up to 480 atoms) depends on the size and temperature of the original particles. Similar simulations were performed by Hawa and Zachariah[30] for hydrogen-neutralized silicon particles in order to investigate possibilities of controlling the size of silicon particles generated through vapor phase. Hawa and Zachariah also developed a mathematical model for the coalescence of coated particles[31] and extended the investigations to coalescence of unequal sized particles.[32] Rogan *et al.*[33] used the embedded atom method (EAM) potential to model binary collisions between small gold clusters and observed fusion, fragmentation, and scattering collision modes. Arcidiacono *et al.*[34] have performed MD simulations of coalescence of solid gold nanoparticles for sintering processes. The clusters were modeled by using the glue potential. They reported that coalescence of gold clusters with radii greater than 20 Å agreed well with macroscopic phenomenological models, whereas for smaller particles the models do not hold.

The aim of the present study is to investigate a variety of phenomena occurring during the binary collision between spherical particles at nanoscale (henceforth called clusters) for a broad range of collision angles and impact speeds. We have employed the molecular dynamics method in conjunction with the 12-6 Lennard-Jones (LJ) interaction potential for modeling the interatomic forces, so that the results are applicable for a range of materials. Each cluster consists of approximately 10 000 atoms, which is about one magnitude bigger than the largest cluster that has been used in previous binary collision studies. We attempt to shed light on the collision dynamics at nanoscales and examine similarities between nanoscales and macroscopic scales. Qualitative comparisons with previous MD studies and analytical prediction models derived for macroscopic droplet collisions are also presented. In addition to the collision identification approaches that have been used in previous MD studies, we propose an alternative identification scheme that enables classification of the collision phenomena into main modes and submodes with respect to different collision angles and impact speeds. Finally, we investigate whether the collision mode referred to as reflexive separation, which has been observed in macroscopic droplet collisions, occurs at nanoscale. The paper is organized as follows. Sections II and III present the molecular dynamics model and definitions of several parameters, respectively, which are used in the analysis of the results. Section IV presents the initial setup of the nanoparticles. The results are discussed in Sec. V including a description of the identification criteria used in the classification of the collision dynamics modes. Comparisons of the present results with previous findings related to macroscale droplets are discussed in Sec. VI. Section VII summarizes the main conclusions of the study.

II. MOLECULAR MODEL AND SIMULATION METHOD

The investigation of collision dynamics phenomena has been carried out using the MD approach.[35] MD calculates the trajectory of a molecular system through phase space. The trajectory data including positions, velocities, and accelerations of all atoms over the simulated time can be processed to study the collision dynamics in detail. MD is a standard tool for cluster simulations and has been employed in several previous investigations of cluster-cluster[23–27,33] and cluster-surface collisions.[36–40]

The clusters of the present study consist of atoms that are modeled by the widely used 12-6 Lennard-Jones (LJ) potential. For two atoms i and j the LJ potential is defined by

$$\mathcal{V}_{ij}^{\mathrm{LJ}}(r_{ij}) = 4\epsilon\left[\left(\frac{\sigma}{r_{ij}}\right)^{12} - \left(\frac{\sigma}{r_{ij}}\right)^{6}\right], \tag{1}$$

where r_{ij} is the distance between the two atoms. Choosing appropriate values for ϵ and σ allows modeling of different materials. The LJ potential models best the van der Waals forces between atoms of noble gases such as argon.

To reduce the computational cost, previous MD studies of clusters, e.g., Ming *et al.*,[25] employed a cutoff distance of $r_c = 2.5 \times \sigma$. However, in a recent study[27] we found that the trajectory is incorrectly altered when using a cutoff distance less than $5 \times \sigma$. Therefore, the distance of $5 \times \sigma$ has been used in the present simulations. To further speed up the simu-

TABLE I. Nondimensionalization based on the atomic mass and the Lennard-Jones potential parameters. The symbol amu denotes the atomic mass unit.

Physical quantity	Factor	Unit for argon
Mass	m_a	39.948 amu
Length	σ	0.341 nm
Energy	ϵ	1.654×10^{-21} J
Time	$\sigma\sqrt{m_a/\epsilon}$	2.16 ps
Velocity	$\sqrt{\epsilon/m_a}$	158 m/s
Angular velocity	$\sqrt{\epsilon/(m_a\sigma^2)}$	0.463 THz
Linear momentum	$\sqrt{m_a\epsilon}$	6.31×10^{3} amu m/s
Angular momentum	$\sigma\sqrt{m_a\epsilon}$	2.15×10^{-6} amu m^2/s
Temperature	ϵ/k_B	119.8 K

lation an neighbor list algorithm has been employed in connection with the cell method.[35,41]

The atomic trajectories are computed using an adaptive predictor-corrector algorithm.[42] Similar to previous investigations,[27] we have used a dimensionless time step of 0.0023. The nondimensionalization is defined according to Table I and is based on the atomic mass m_a and the Lennard-Jones parameters σ and ϵ. For the case of argon, these parameters take the values $m_a=39.948$ amu (Refs. 25 and 27) and $\epsilon=1.654\times10^{-21}$ J, $\sigma=0.341$ nm.[35]

III. DEFINITIONS

Different criteria have been used for analyzing the computed trajectories. Collision fragments that are formed during the collision process are classified according to their size. The absolute size, S^α, of a fragment α is defined as the number of atoms of the fragment. The relative size, s^α, is the number of atoms of fragment α relative to the initial number of atoms in one cluster N ($s^\alpha=S^\alpha/N$). Using the relative size, fragments have been classified into four categories: very large, large, medium, and small (Table II). The largest fragment is labeled as F^1 with a relative size s^1; the second, third, and N_fth largest fragments are labeled as $F^2,F^3,\ldots,F^{N_f}$ with relative size $s^2,s^3,\ldots,s^{N_f}$.

Depending on the collision dynamics, there may be one or two main fragments. We define as scattered atoms all atoms that do not belong to the main fragments,

$$N_{\mathrm{sca}}=\begin{cases}2N-S^1, & \text{one main fragment},\\ 2N-(S^1+S^2), & \text{two main fragments}.\end{cases} \tag{2}$$

TABLE II. Classification of fragments according to their size; s and S are the relative and absolute size of the fragments, respectively.

Type	Abbreviation	s	S
Very large	F_{vl}	$10\%\leqslant s$	$1000\leqslant S$
Large	F_l	$1\%\leqslant s<10\%$	$100\leqslant S<1000$
Medium	F_m	$0.1\%\leqslant s<1\%$	$10\leqslant S<100$
Small	F_s	$s<0.1\%$	$S<10$

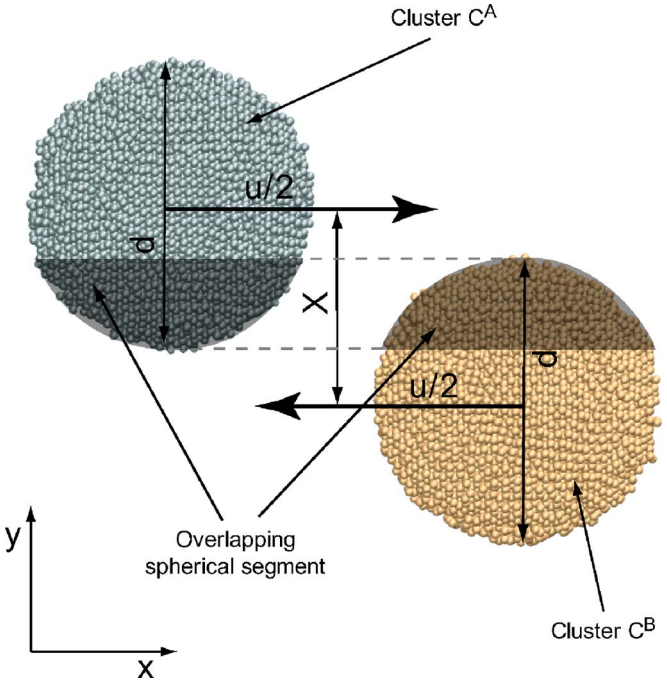

FIG. 1. (Color online) Initial setup of the binary nanoclusters. Both clusters are assigned a speed of $u/2$ in opposite direction. The right cluster is displaced by X in the negative y direction.

For the identification of fragments the nearest-neighbor distance criterion of Stoddard[43] has been applied with a critical atom separation of $r_{cl}=1.76$. A description of the fragments' detection algorithm can be found in Ref. 27.

The analysis of collision dynamics involves the calculation of several fragment and cluster properties; henceforth, the word fragment will apply to clusters as well. For a fragment F^α the center $\boldsymbol{r}^\alpha$ is considered as the center of mass. The translational and angular velocities are $\boldsymbol{v}^\alpha$ and $\boldsymbol{\omega}^\alpha$, respectively. $\boldsymbol{\omega}^\alpha$ is calculated from angular momentum $\boldsymbol{l}^\alpha$ and the inertia tensor $\mathbf{I}^\alpha$. In the analysis, we have considered both internal and external energies. The internal potential energy $E^\alpha_{p,\mathrm{int}}$ of a fragment F^α is calculated by the sum of the interactions between the atoms within the cluster. Furthermore, the internal, $E^\alpha_{k,\mathrm{int}}$, and external, $E^\alpha_{k,\mathrm{ext}}$, kinetic energies are used in the analysis of the results. $E^\alpha_{k,\mathrm{int}}$ comprises the linear, $E^\alpha_{kl,\mathrm{ext}}$, and the angular, $E^\alpha_{ka,\mathrm{ext}}$, parts. The calculation of these

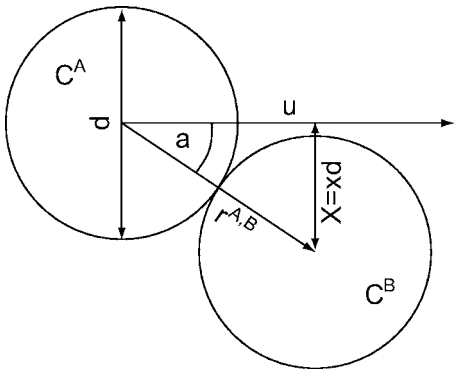

FIG. 2. Relation of impact factor x and collision angle α.

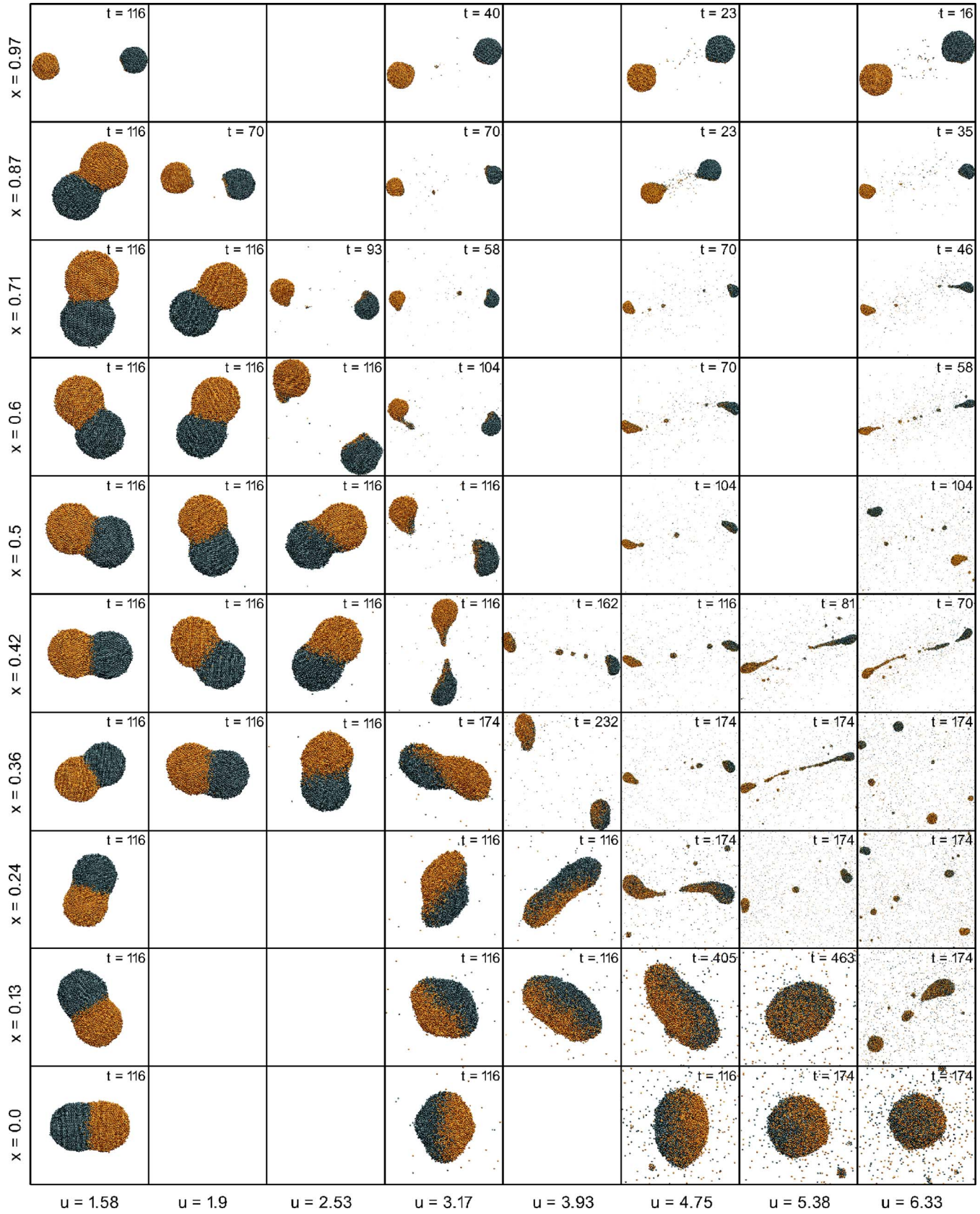

FIG. 3. (Color online) *x-u* matrix showing an overview of collision outcomes for different impact factors and velocities. The scale varies between the individual images because the distribution of material in space is different in each case (see Figs. 4–6 for classification of modes and submodes). All numbers are nondimensional.

TABLE III. Nondimensional times at which the fragment parameters were calculated (see Tables IV–VI).

$x\backslash u$	1.58	1.9	2.53	3.17	3.93	4.75	5.38	6.33
0.00	116			116		116	174	174
0.13	116			116	116	174	174	174
0.24	116			116	116	174	290	174
0.36	116	116	116	116	290	174	232	174
0.42	116	116	116	116	174	116	232	116
0.50	116	116	116	116		116		116
0.60	116	116	116	116		116		116
0.71	116	116	116	116		116		116
0.87	116			116		116		116
0.97	116			35		35		116
1.00	116			35		35		35

variables is standard mechanics and can be found in standard textbooks, e.g., Goldstein *et al.*[44]

The fragments' temperature are obtained from the internal kinetic energy by

$$T^{\alpha} = \frac{2E^{\alpha}_{k,\mathrm{int}}}{k_B f^{\alpha}}, \tag{3}$$

where k_B is Boltzmann constant and f^{α} are the degrees of freedom of the fragment; $f^{\alpha}=3S^{\alpha}-6$ for an atomic fragment.

IV. SETUP OF NANOCLUSTERS

The initial setup for the two binary clusters, C^A and C^B, is shown in Fig. 1. Each cluster consists of $N=10\,973$ atoms, has a diameter of $d\approx 27$, a temperature of 0.33, and an internal potential energy of $E_{p,\mathrm{int}}\approx 8\times 10^4$. They have been spherically cut from a face-centered cubical crystal and equilibrated over 100 000 time steps.

The collision dynamics is investigated with respect to relative speed u and impact parameter X. The absolute velocities are given by

TABLE IV. Relative size of the largest fragment, s^1, for different collision speeds, u, and impact factors, x.

$x\backslash u$	1.58	1.9	2.53	3.17	3.93	4.75	5.38	6.33
0	100.0			99.5		90.7	78.2	58.7
0.13	100.0			99.5	98.4	89.5	77.0	39.6
0.24	100.0			99.6	98.8	48.8	38.5	20.8
0.36	100.0	100.0	99.9	99.7	48.9	43.1	35.8	26.1
0.42	100.0	100.0	99.9	51.3	47.3	45.0	44.6	32.7
0.5	100.0	100.0	99.9	50.4		47.2		40.2
0.6	100.0	100.0	50.1	50.5		47.8		44.2
0.71	100.0	100.0	50.7	49.7		47.8		47.4
0.87	100.0	50.1		49.7		49.8		49.3
0.97	50.1			50.0		49.9		49.9
1	50.0			50.0		50.0		50.0

TABLE V. Relative size of the second largest fragment, s^2, for different collision speeds, u, and impact factors, x.

$x\backslash u$	1.58	1.9	2.53	3.17	3.93	4.75	5.38	6.33
0.00	0			0		1.1	1.5	3.8
0.13	0			0	0	1.3	4.8	17.6
0.24	0			0	0	41.4	29.1	20.4
0.36	0	0	0	0	47.4	43.1	33.1	22.6
0.42	0	0	0	48.1	45.8	43.5	42.0	32.7
0.50	0	0	0	48.4		37.0		38.8
0.60	0	0	49.8	48.9		46.9		42.5
0.71	0	0	49.0	48.8		47.8		47.0
0.87	0	49.9		49.5		49.8		49.2
0.97	49.9			49.9		49.9		49.8
1.00	50.0			50.0		50.0		49.9

$$\boldsymbol{v}^A = \frac{1}{2}\begin{pmatrix} u \\ 0 \\ 0 \end{pmatrix}, \quad \boldsymbol{v}^B = -\frac{1}{2}\begin{pmatrix} u \\ 0 \\ 0 \end{pmatrix}, \tag{4}$$

for the clusters C^A and C^B, respectively. The linear momentums are $\boldsymbol{p}^A=Nm_a\boldsymbol{v}^A$ and $\boldsymbol{p}^B=Nm_a\boldsymbol{v}^B$; the initial relative momentum is $\boldsymbol{p}=2Nm_a\boldsymbol{u}$; and the total linear momentum is $\boldsymbol{p}_t=\boldsymbol{p}^A+\boldsymbol{p}^B=0$.

The impact parameter, X, determines how far off-center the collision occurs and is defined as the distance from the center of one cluster to the relative velocity vector $\boldsymbol{u}$ originating from the center of the other cluster.[1] Nondimensionalizing X yields x that can be easily related to the collision angle α (Fig. 2),

$$x = \frac{X}{d}, \quad x = \sin(\alpha). \tag{5}$$

For $x=0$ ($\alpha=0°$) both clusters are subject to head-on collision, whereas for $x=1$ ($\alpha=90°$) the collision is marginally avoided.

TABLE VI. Values of $s^{|1-2|}$, for different collision speeds, u, and impact factors, x.

$x\backslash u$	1.58	1.9	2.53	3.17	3.93	4.75	5.38	6.33
0	100.0			99.5		89.6	76.7	54.9
0.13	100.0			99.5	98.4	88.3	72.2	22.1
0.24	100.0			99.6	98.8	7.5	9.4	0.4
0.36	100.0	100.0	99.9	99.7	1.5	0	2.7	3.7
0.42	100.0	100.0	99.9	3.1	1.4	1.5	2.6	0.1
0.5	100.0	100.0	99.9	2.0		10.3		1.4
0.6	100.0	100.0	0.4	1.6		0.9		1.6
0.71	100.0	100.0	1.7	0.9		0		0.5
0.87	100.0	0.2		0.2		0		0.1
0.97	0.2			0.1		0		0.1
1	0			0		0		0

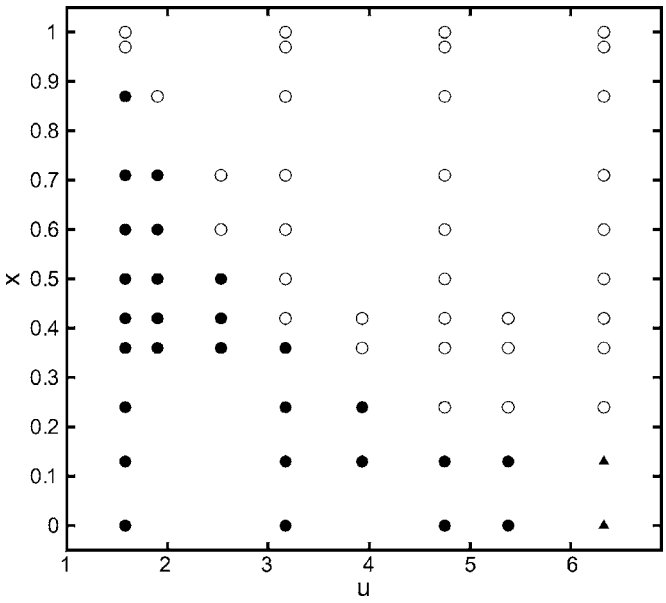

FIG. 4. Collision modes depending on the impact factor, x, and velocity, u, based on the identification schemes A. Coalescence is denoted by (●), stretching separation by (○), and shattering by (▲).

The displacement X must be perpendicular to the relative velocity vector $\boldsymbol{u}$ that is aligned to the horizontal direction. Therefore, the right cluster is moved by X in the negative y-direction and the two initial positions of C^A and C^B are set as

$$\boldsymbol{r}^A = \frac{1}{2}\begin{pmatrix} -17 \\ 0 \\ 0 \end{pmatrix}, \quad \boldsymbol{r}^B = \frac{1}{2}\begin{pmatrix} 17 \\ -X \\ 0 \end{pmatrix}. \tag{6}$$

For $x \neq 0$ an angular momentum $\boldsymbol{l}$ in the z direction is introduced, which is conserved throughout the simulation,

$$\boldsymbol{l}_z = \tfrac{1}{2} N m_a u x. \tag{7}$$

V. INVESTIGATION OF COLLISION DYNAMICS

The collision dynamics of two LJ_{10973} clusters was investigated for different values of the impact parameter x in the range of 0 to 1 and at different speeds, u, in the range of 1.58 to 6.33 (nondimensional). Initially, simulations were carried out for all combinations of $x = \{0, 0.13, 0.24, 0.36, 0.42, 0.5, 0.6, 0.71, 0.87, 0.97, 0.99\}$ and $u = \{1.58, 3.17, 4.75, 6.33\}$, in order to identify the main collision modes. Furthermore, simulations were performed for selected x and u, to obtain a clearer understanding of the transition between the collision modes and to render more precisely the location of the transition lines. Simulations were conducted for up to 100 000 time steps (a nondimensional time interval of 232). For $x = 0.13$ and $u = 5.33$ computations were performed for 250 000 time steps (a nondimensional time of 580) in order to investigate the evaporation processes that follow a collision with relatively high energy.

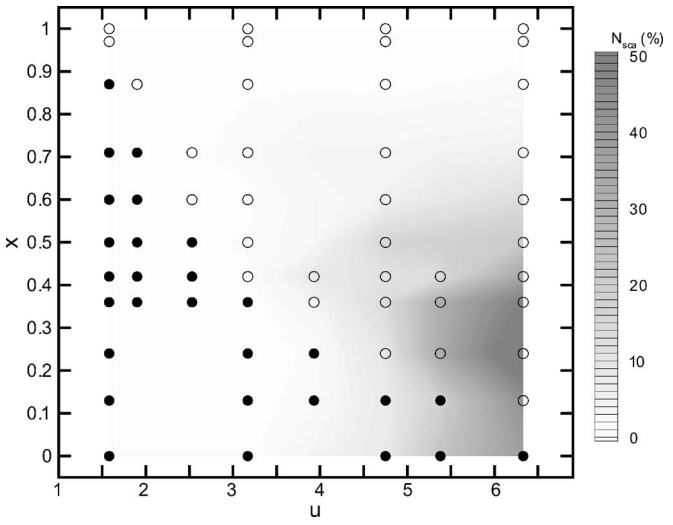

FIG. 5. Collision modes depending on the impact factor, x, and velocity, u, based on the identification schemes B. Coalescence is denoted by (●), stretching separation by (○). The shaded area displays the strength of scattering.

The trajectories have been visualized by using the VMD software.[45]

During the simulation we monitored the state of fragmentation, i.e., number of very large, N_f^{vl}, large, N_f^l, medium, N_f^m, and small fragments, N_f^s; the number of atoms in each class N_a^l, N_a^b, N_a^m, N_a^s; and the number of scattered atoms, N_{sca}. Other parameters were recorded in relation to the two largest fragments F^1 and F^2 including the total sizes, S^1 and S^2; the relative sizes, s^1 and s^2; the fragments' positions, $\boldsymbol{r}^1$ and $\boldsymbol{r}^2$; the velocities, $\boldsymbol{v}^1$ and $\boldsymbol{v}^2$; their angular velocities, $\boldsymbol{l}^1$ and $\boldsymbol{l}^2$; the linear external kinetic energies, $E^1_{kl,\text{ext}}$ and $E^2_{kl,\text{ext}}$; the angular external kinetic energies, $E^1_{ka,\text{ext}}$ and $E^2_{ka,\text{ext}}$; the internal kinetic energies, $E^1_{k,\text{int}}$ and $E^2_{k,\text{int}}$; the internal potential energies, $E^1_{p,\text{int}}$ and $E^2_{p,\text{int}}$; the external potential energies, $E^1_{p,\text{ext}}$ and $E^2_{p,\text{ext}}$; and the temperatures, T^1 and T^2.

An overview of the collision dynamics for different impact factors, velocities, and times is shown in Fig. 3. The

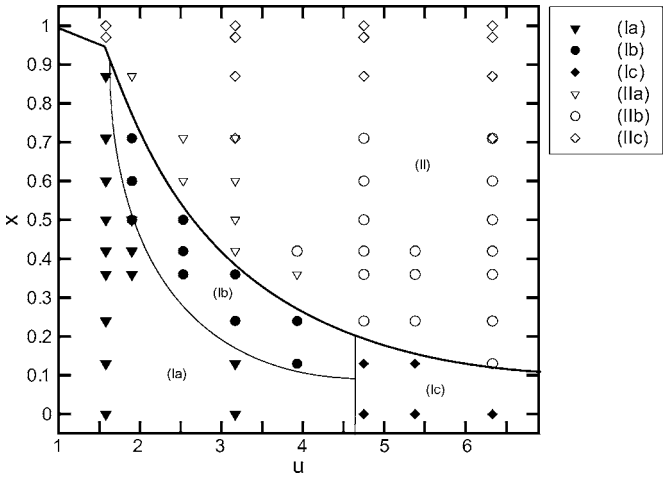

FIG. 6. Overview of the collision modes including submodes in x-u space: (Ia) sticking; (Ib) sliding and locking; (Ic) droplet; (IIa) normal stretching separation; (IIb) stretching separation with satellite droplets; (IIc) shearing off.

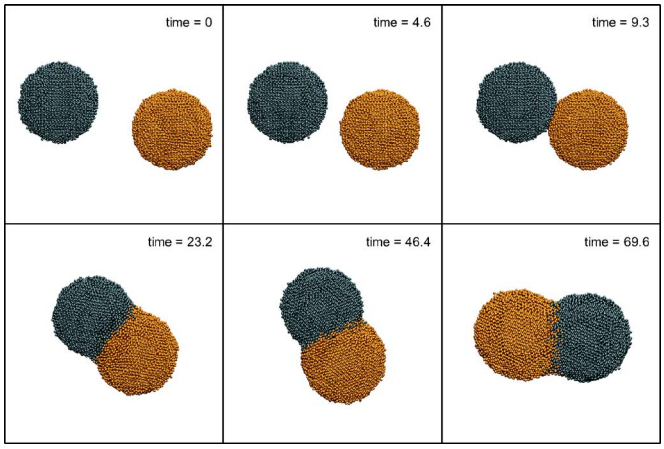

FIG. 7. (Color online) Collision typical to coalescence mode (x=0.36, u=1.58) with the resulting cluster taking a dumb-bell shape.

scale varies between the images in order to enable visualization of the spatial distribution of the resulting fragments. For low x and/or low u the collision results in one main fragment whose shape depends on the x and u values. This collision mode is referred to as *coalescence* [henceforth labeled as (I)]. For higher x and/or u values the collision yields two main fragments and in some cases it may also include satellite droplets. As it will be described later in more detail, the temporarily formed cluster separates after being stretched, thus the mode is referred to as *stretching separation* [labeled as (II)]. A third collision mode, *shattering* [labeled as (III)], which corresponds to the destruction of both clusters, occurs for high velocities, u, in connection with low impact factors, x. In the following section, classification of the collision modes is presented in detail.

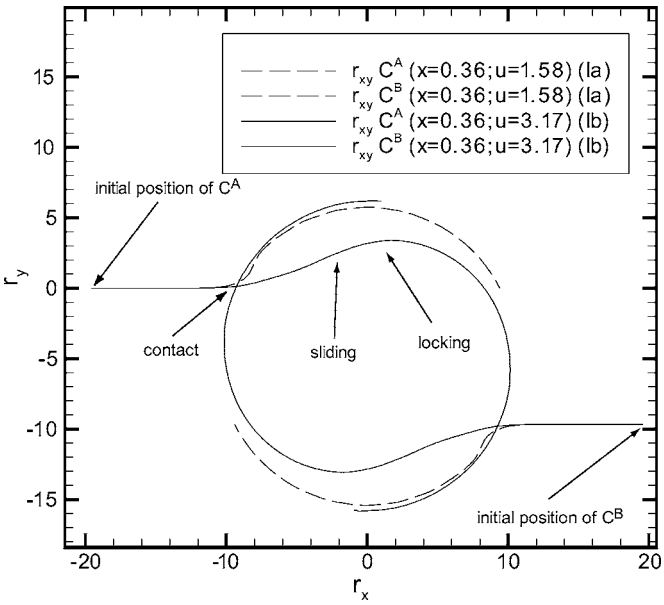

FIG. 8. Trajectories of the mass centers r^A and r^B for coalescence mode, sticking (Ia) and slide-and-locking (Ib) submodes; C^A and C^B trajectories start on the left and right sides, respectively, and are traced for t=0–116 (nondimensional).

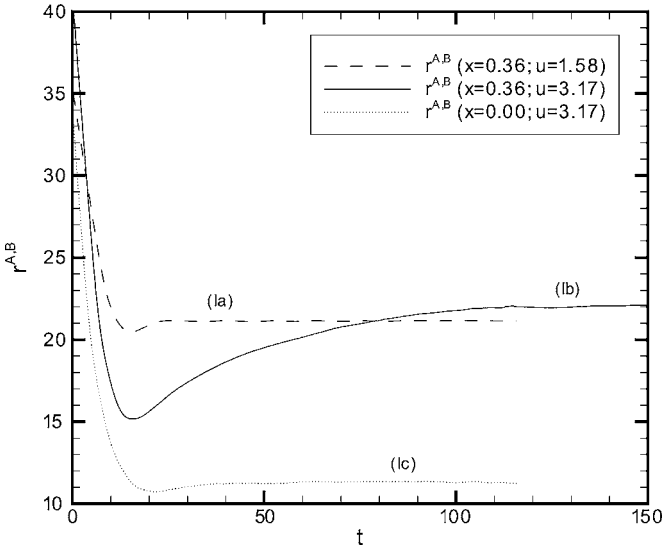

FIG. 9. Distance $r^{A,B}$ between the centers of mass r^A and r^B of the original clusters C^A and C^B for sticking (Ia); sliding and locking (Ib); and droplet (Ic) submodes.

A. Modes classification

Different techniques and criteria can be used for identifying the collision modes. One possibility is to classify the dynamics visually as done in experiments.[1] The same procedure can be used in the context of MD simulations and, additionally, one can obtain a more thorough analysis of the dynamics using the computed trajectories. To identify the collision modes the following parameters were employed: the relative size of the largest, s^1, and second largest fragment, s^2; and the difference of the relative sizes of the two largest fragments $s^{|1-2|}=|s^1-s^2|$. These parameters are calculated at different times (Table III) depending on the duration of the collision. The values of these parameters for different impact factors and velocities are given in Tables IV–VI.

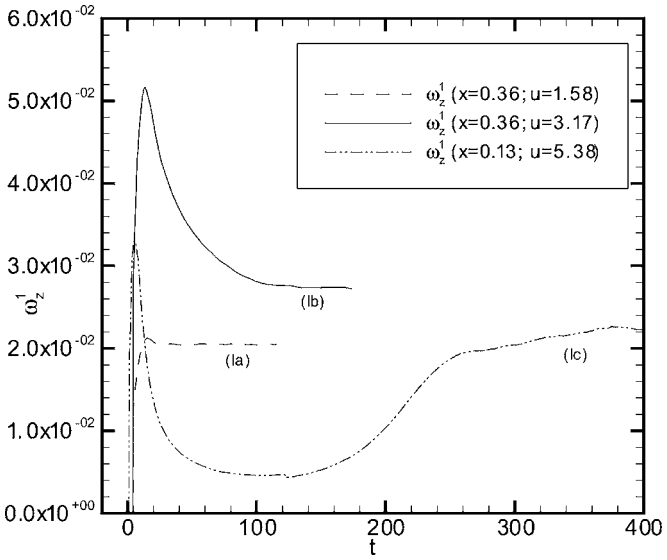

FIG. 10. Angular velocity ω_z^1 of the resulting cluster at late time for sticking (Ia); sliding and locking (Ib); and droplet (Ic) modes.

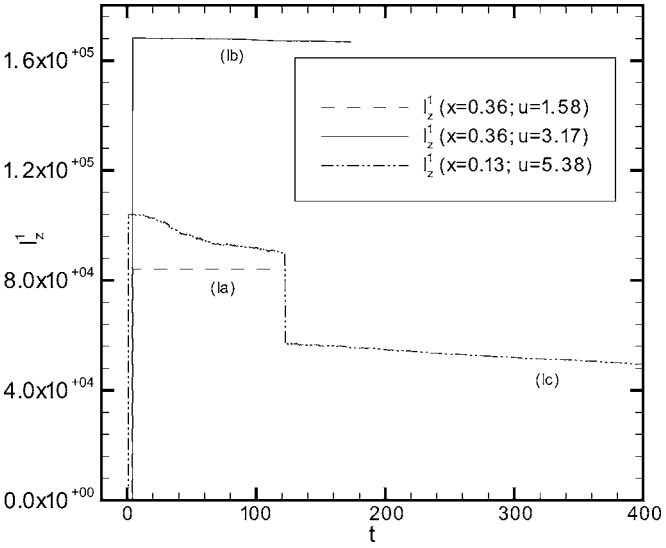

FIG. 11. Angular momentum l_z^1 of the cluster at late time for sticking (Ia); sliding and locking (Ib); and droplet (Ic) submodes.

Identification scheme A: One possibility is to adapt the scheme used by Ming *et al.*,[25] which compares s^1 and s^2 with threshold values $c_{A1}=70\%$ and $c_{A2}=20\%$, respectively. These values provide the best agreement with the visualizations. The collision modes can then be classified as

(I) Coalescence for $s^1 > c_{A1}=70\%$.

(II) Stretching separation for $s^2 > c_{A2}=20\%$.

(III) Shattering for $s^1 < c_{A1}=70\%$ and $s^2 > c_{A2}=20\%$.

Even though these criteria allow, in theory, a collision to belong simultaneously in coalescence and stretching separation modes, none of the simulated cases resulted in this scenario. Applying the above criteria in conjunction with the computed s^1 (Table IV) and s^2 (Table V) yields the collision modes of Fig. 4. The transition between coalescence and stretching separation is clearly identified. The shattering mode is somewhat arbitrarily defined due to the diffusive nature of the transition towards shattering compared to the other two collision modes.

Identification scheme B: This scheme uses $s^{|1-2|}$, i.e., the size difference of the largest and second largest fragment, to distinguish between coalescence and stretching separation modes based on a threshold value, $c_2=15\%$. It also examines the percentage of scattered atoms N_{sca}/N instead of defining the shattering mode. The criteria for scheme *B* are listed as follows:

(I) Coalescence for $s^{|1-2|} > c_B=15\%$.

(II) Stretching for $s^{|1-2|} < c_B=15\%$.

Figure 5 demonstrates application of the above criteria on the present MD results. The shading denotes the intensity of scattering (N_{sca}/N), where the dark areas correspond to strong scattering. The collision dynamics discussed in the next sections is based on the identification scheme *B*. The boundaries between the collision modes are shown in Fig. 6 including various submodes, which are explained in detail in the following sections.

B. Coalescence (I)

Generally, the coalescence mode prevails at low velocities, u, and/or small impact parameters, x. Common to all collisions belonging to this mode is the formation of one main cluster or a droplet that is created by the two original clusters. Scattering of atoms occurs only at high velocities. The structure, shape, temperature, and motion of the final aggregate as well as the dynamics of the collision process differ within the coalescence mode. The present simulations revealed three different submodes: (a) *sticking mode*, (b) *slide and locking mode*, and (c) *droplet mode*. The locations of these submodes are illustrated in the x-u diagram of Fig. 6. Transition between submodes occurs gradually, thus collisions occurring in the vicinity of borderlines encompass features of two different submodes.

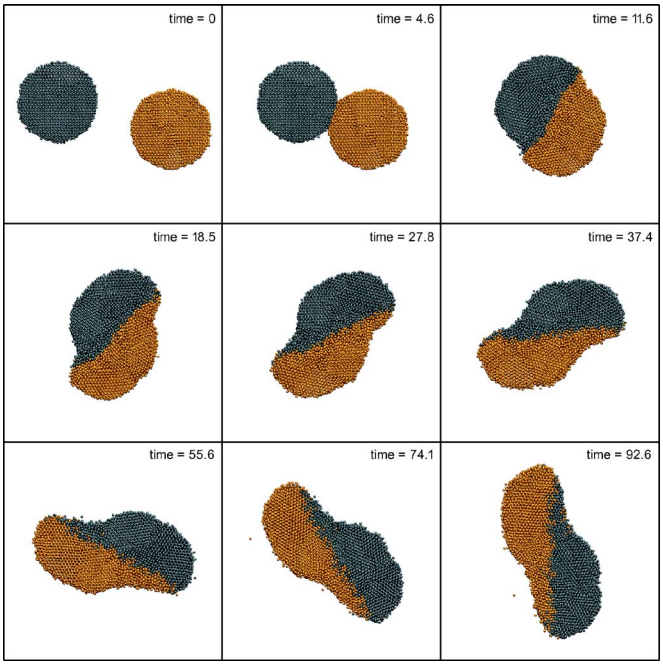

FIG. 12. (Color online) Development of coalescence featuring slide-and-locking mode ($x=0.36$, $u=3.17$).

1. Sticking mode (Ia)

Figure 6 shows that for $u<1.58$ the sticking submode covers the entire range of impact factor x, except for $x>0.87$, where the collision results in both clusters sticking together, while their internal structures remain intact. The shape of the resulting cluster resembles that of a dumb-bell (Fig. 3) thus it is also referred to as dumb-bell mode.[23]

The collision dynamics of a typical (Ia) case, e.g., $x=0.36$ and $u=1.58$, is shown in Fig. 7. During impact, only the material near the contact interface is deformed. Once the dumb-bell cluster is created, the two clusters are locked to each other. The translational motion is transformed into rotation. The trajectories of the two original clusters, C^A and C^B, are plotted in Fig. 8, starting on the left-hand side for C^A and on the right-hand side for C^B, respectively. For the sticking mode case ($x=0.36$, $u=1.58$) the initially straight path is followed by a circular one (dashed line in Fig. 8). The point at which the motion changes is marked as the contact point and this is exactly the position where the two clusters come into contact. The transition from linear to circular motion

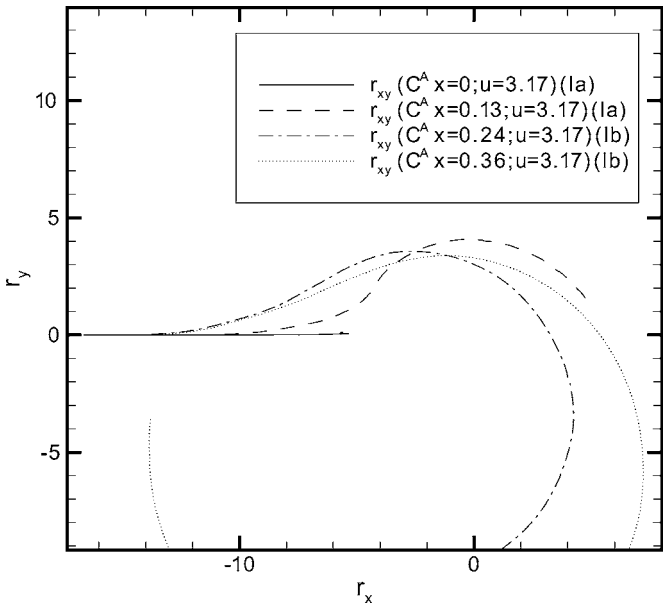

FIG. 13. Trajectories of the clusters C^A for $u=3.17$ and different impact factors x. For $x=\{0,0.13\}$ the collision belongs to sticking mode (Ia), while for $x=\{0.24,0.36\}$ belongs to slide-and-locking mode (Ib).

occurs in a very short period of time. The distance between the mass centers of the two initial clusters, $r^{A,B}$, remains constant after the clusters have come in contact with each other (Fig. 9).

Figures 10 and 11 show the variation of the angular velocity ω_z^1 and angular momentum l_z^1 in time of the dumb-bell cluster F^1. Before the initial clusters come in contact there is no rotation. Following impact, the angular momentum, w_z^1, steeply rises and reaches a plateau value, while, as expected, the angular momentum l_z of the resulting cluster is conserved (Fig. 11).

For impact factors $x<0.2$ the collision can still be characterized as sticking mode, even for velocities $u>2$, with the original clusters being flattened at impact. The dumb-bell shape appearing at lower u is replaced by an elliptical or a spherical shape. A typical example is the collision for $x=0$ and $u=3.17$ (Fig. 3). The change of $r^{A,B}$ is shown in Fig. 9. The distance between the cluster centers is smaller compared to the case of ($x=0.13$, $u=1.58$). By increasing further the impact velocity ($u>4$), the collision mode will gradually change to the droplet mode. The collision in sticking mode is governed by transformation of the initial external linear kinetic energy $E_{kl,\mathrm{ext}}$ into internal kinetic energy $E_{k,\mathrm{int}}$, internal potential energy $E_{p,\mathrm{int}}$ corresponding to the structural changes of the deformation, and angular kinetic energy $E_{ka,\mathrm{ext}}$.

2. Slide-and-locking mode (Ib)

The slide-and-locking mode forms a narrow (transition) region in x-u space between coalescence and stretching separation (Fig. 6). The collision dynamics for a typical case ($x=0.36$, $u=3.17$) is shown in Fig. 12. The clusters are flattened at impact ($t=4.6-11.6$) and the initial contact point

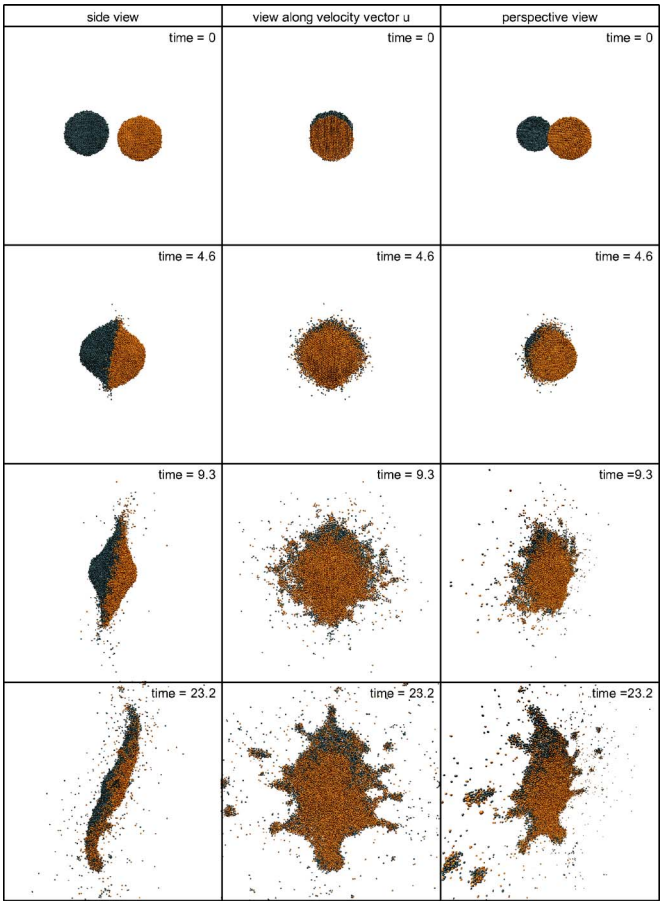

FIG. 14. (Color online) Collision dynamics in coalescence-droplet mode with strong scattering and evaporation, for $x=0.13$ and $u=5.33$.

evolves to a flat circular interface. The heat generated at the contact interface liquifies the material in this region and a (liquid) layer with reduced friction is formed acting as a cushion between the clusters facilitating sliding along each other. The direction of the clusters' motion is slightly deflected outwards and aligns parallel to the contact interface. During sliding the heat is dissipated away from the interface to the rest of the cluster thus cooling down the interface and increasing friction. The linear motion is transformed into rotation of the entire complex. Eventually, the interface locks and the sliding motion completely stops leaving behind a rotating cluster. The shape of the resulting cluster depends mainly on the extent of flattening and sliding of the original cluster.

The motion of the clusters can be traced by plotting the position of the mass centers projected onto a two-dimensional plane [solid line, (Ib) case in Fig. 8], where the contact and locking points as well as sliding area are shown. After the initial contact the clusters' trajectories remain parallel to each other, while symmetry is preserved throughout. As the friction increases, the trajectories enter a circular motion and the contact interface is locked thus not permitting further sliding of the clusters. The distance of the mass centers, $r^{A,B}$ (Fig. 9), shows that the closest approach occurs immediately after the clusters have come in contact. The

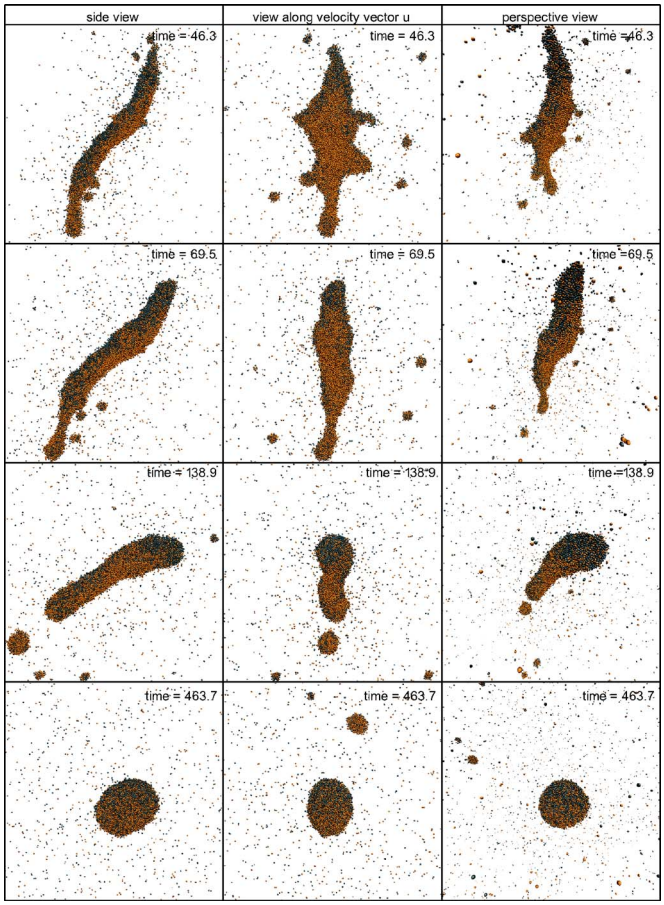

FIG. 15. (Color online) Continuation of Fig. 14. Collision dynamics in coalescence-droplet mode with strong scattering and evaporation, for $x=0.13$ and $u=5.33$.

distance $r^{A,B}$ increases during the sliding phase and approaches asymptotically a plateau value as sliding continues. The angular momentum, l_z^1, of the formed cluster is conserved (Fig. 11) and the angular velocity, ω_z^1, decreases (solid

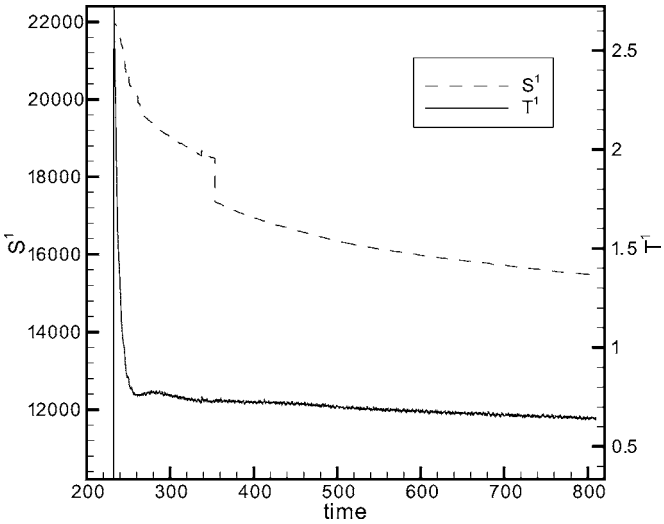

FIG. 16. Size and temperature of the largest fragment for the case of $x=0.13$ and $u=5.38$ [droplet mode (Ic)].

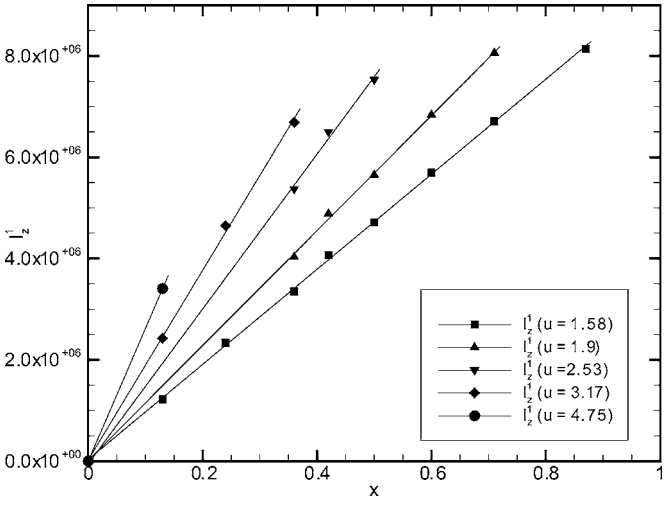

FIG. 17. Angular momentum l_z^1 of the largest fragment F^1 against the impact factor x for collisions in coalescence mode.

lines in Figs. 9 and 10). The initial, linear kinetic energy, $E_{kl,\mathrm{ext}}$, is transformed into: (i) internal potential energy, $E_{p,\mathrm{int}}$, causing deformation and increasing pressure; and (ii) internal kinetic energy, $E_{k,\mathrm{int}}$, in the vicinity of the contact interface. During the sliding-and-locking phase, the remaining part of $E_{kl,\mathrm{ext}}$ is transformed into $E_{k,\mathrm{int}}$ and angular kinetic energy, $E_{ka,\mathrm{ext}}$, of the entire cluster.

Increasing the velocity u results in faster and longer sliding motion, which eventually leads to the separation of both clusters; this is the transition to stretching separation mode. Higher values of x entail a smaller contact interface. Consequently, the transformation of impact energy, $E_{kl,\mathrm{ext}}$, into heat, $E_{k,\mathrm{int}}$, and deformation, $E_{p,\mathrm{int}}$, takes place slower and therefore leads to stretching separation.

We further comment on how the classification of sticking mode (Ia) and slide-and-locking modes (Ib) has been obtained. The trajectories of the two clusters are projected onto a two-dimensional (x-y) plane and if the path follows a straight line after the clusters come in contact, the collision

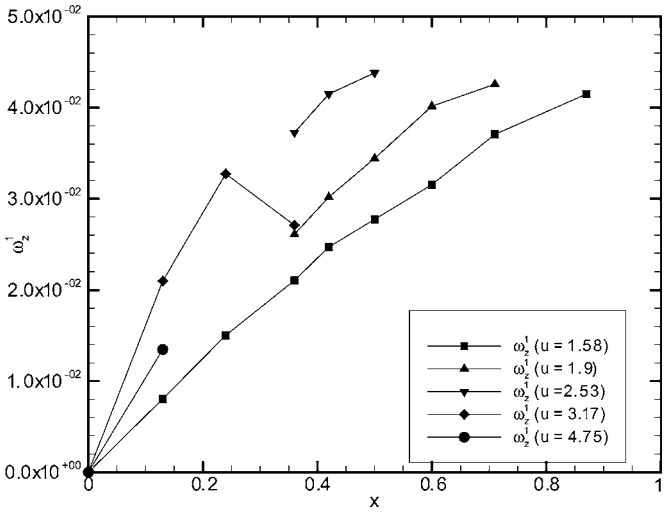

FIG. 18. Angular velocity ω_z^1 of the largest fragment F^1 against the impact factor x for collisions in coalescence mode.

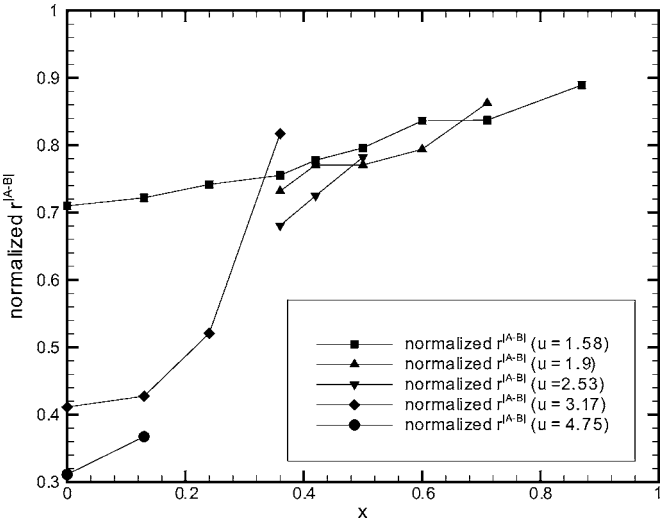

FIG. 19. Normalized distance of the cluster centers $r^{|A-B|}$, i.e., of the two original clusters C^A and C^B inside the resulting cluster F^1 against the impact factor x for collisions in coalescence mode.

mode is considered to be (Ib), otherwise it is classified as (Ia). An example is given in Fig. 13 for constant $u=3.17$ and increasing x. Because the trajectories of C^A and C^B are symmetrical, only those of C^A are displayed. The path for $x=0.0$ is a straight line (central collision), but because there is no sliding, the collision is characterized as (Ia). The path for $x=0.13$ shows no distinct linear section and is therefore considered to belong to mode (Ia). Note that the short straight line is due to compression and flattening of the cluster, thus it does not account for sliding. Increasing the values of x to 0.24 and 0.36, a distinct linear segment can be found in the trajectories following the contact point. Hence, both cases are regarded as mode (Ib). The classification of the collision modes was also checked by examining simulation movies created using the computed trajectories.

3. Droplet mode (Ic)

For impact factors $x<0.2$ and velocities u greater than approximately 4.5 the collision dynamics is classified as droplet mode (Fig. 6). The high impact energy results in one main fragment in liquid phase. In contrast to the previous cases where the original clusters can still be identified within the newly formed aggregate, in the droplet mode the material of the two initial clusters is mixed. The droplet mode also involves significant scattering and evaporation as can be seen from Tables IV–VI.

The collision dynamics for a typical example ($x=0.13$ and $u=5.33$) is shown in Figs. 14 and 15, where each column shows a different view: from the side (along the z axis), along the velocity vector **u**, and from a perspective view. The clusters are flattened along a planar contact interface ($t=4.6$). Radial, disclike scattering originating from the contact interface is observed at $t=4.6$ and $t=9.3$. The scattering is due to the transformation of the largest part of impact energy into heat at the contact interface. The internal pressure force acts outwards and is opposed by an inward pressure force due to the interatomic and deceleration forces.

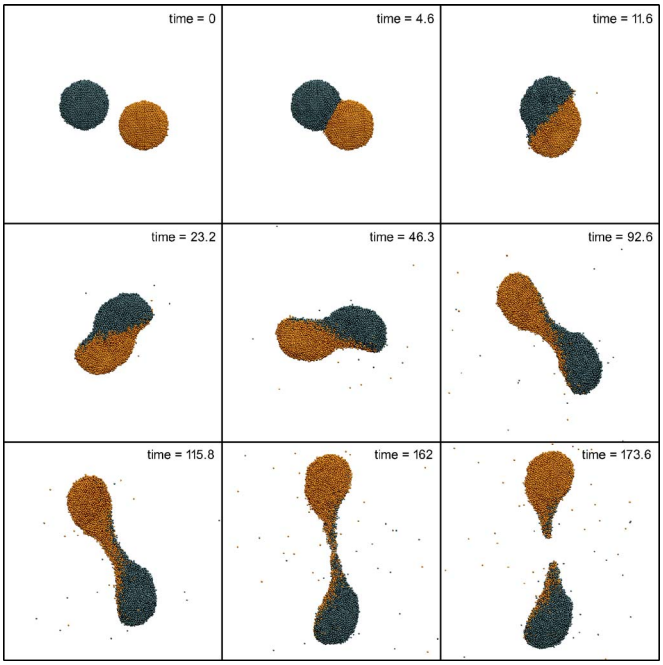

FIG. 20. (Color online) Collision dynamics in normal stretching separation mode (IIa) for $x=0.42$ and $u=3.17$.

Because the pressure acting perpendicular to **u** is much smaller than the one acting in the direction of **u** the contact interface expands radially. The expansion overcomes the binding forces and results in asymmetric scattering, which reaches a peak value at $t\approx 14$. While the contact interface widens out into a circular plane, asymmetric momentum distribution forces the planar interface to bend and take an S-like shape (see, e.g., side view at $t=23.2$ in Fig. 14). The onset of this behavior is already visible in the slide-and-locking case (Fig. 12). At later times an elongated droplet is formed ($t=138.9$ in Fig. 15), which finally approaches a spherical shape (last row of Fig. 15).

During the collision process, evaporation and condensation of the liquid and gas atoms, respectively, occur. The process leads gradually to reduced size and temperature of the formed droplet, while the evaporation rate is also gradually reduced. The effect of evaporation is encountered by condensation of the vapor phase surrounding the droplet. When the rate of evaporation equals the rate of condensation an equilibrium is achieved. To examine evaporation and confirm the spherical shape of the final fragment, we have extended the simulations for $x=0.13, u=5.38$ until $t=925$. The change of absolute size S^1 and temperature T^1 of the largest fragment, F^1, are shown in Fig. 16. The initial stages are dominated by scattering and from $t=34$ onwards the decay in S^1 is caused by evaporation. The sudden change at $t=122$ is due to the separation of a satellite droplet; cf. $t=69.5$ and $t=138.9$ in Fig. 15. The reduction of the absolute size S^1 shows an asymptotic behavior towards the end of the simulation.

4. Effects of the impact factor x

We have investigated the dependence of angular momentum, angular velocity, and distance of the clusters centers' on

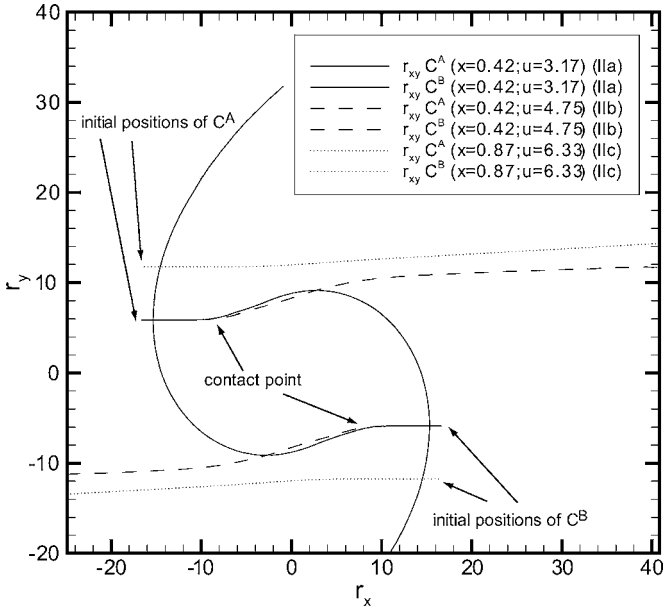

FIG. 21. Trajectories of the clusters C^A and C^B for the (IIa), (IIb), and (IIc) submodes.

the impact factor x. According to (7) the angular momentum of the final fragment is determined by the initial setup. The l_z^1 values obtained from the simulations are shown in Fig. 17 and agree exactly with the values calculated by (7), i.e., follow a linear variation with slope $\frac{1}{2}Nm_a u$. Because the angular momentum is conserved the angular velocity ω_z^1 depends only on the shape of the final fragment. Figure 18 shows that larger impact factors result in larger ω_z^1. Deviation from this behavior is observed for $u=3.17$ and $x=0.36$ because of the slide-and-locking effect (cf. Fig. 12), which results in high values of $\mathbf{I}_{zz}$, due to the elongated shape of the formed cluster. The angular velocity, ω_z^1, depends on the inertia of the main fragment, F^1, thus depending on $r^{A,B}$. The normalized distance $r^{|A,B|}$ (normalization factor is $1/d$) between the clusters' centers is plotted in Fig. 19. For low velocities, $u=1.58, 1.9$, $r^{|A,B|}$ follows a linear dependency on x. At higher values (e.g., for $u=3.17$) the effect of sliding reflects on the steep increase of $r^{|A,B|}$, especially for higher x.

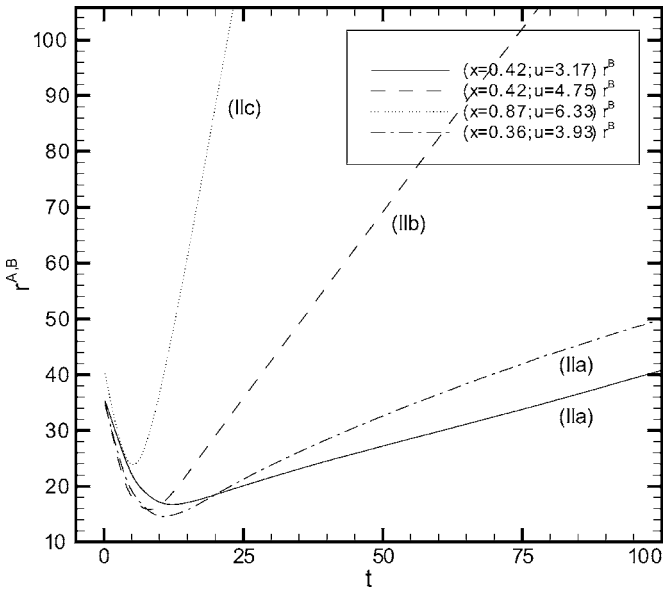

FIG. 22. Distance $r^{A,B}$ between the mass centers r^A and r^B of the original clusters C^A and C^B as a function of time for collision dynamics in stretching separation modes (IIa), (IIb), and (IIc); see text for more details.

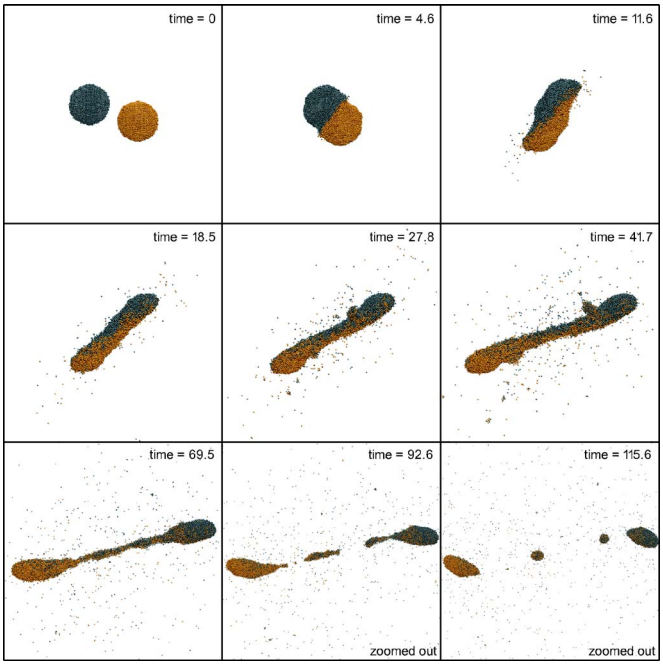

FIG. 23. (Color online) Collision dynamics for $x=0.42$ and $u=4.75$; the case belongs to stretching separation mode with satellite droplets (IIb).

C. Stretching separation (II)

In stretching separation the common fragment, i.e., the cluster or droplet that is temporarily formed by the two original clusters, separates again into two main fragments and, possibly, into additional satellite fragments. Stretching sepa-

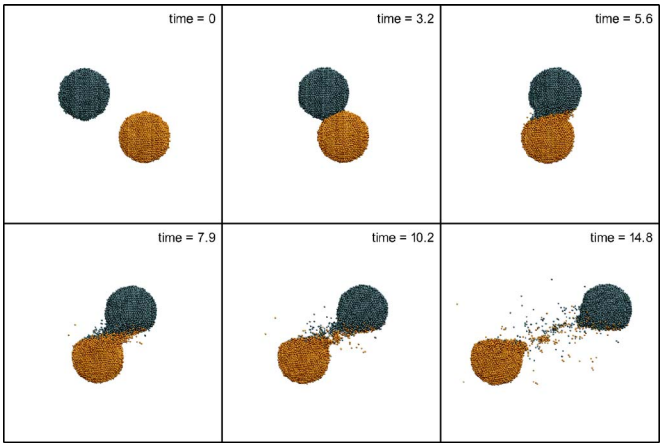

FIG. 24. (Color online) Collision dynamics for the shearing-off case ($x=0.87$, $u=6.33$).

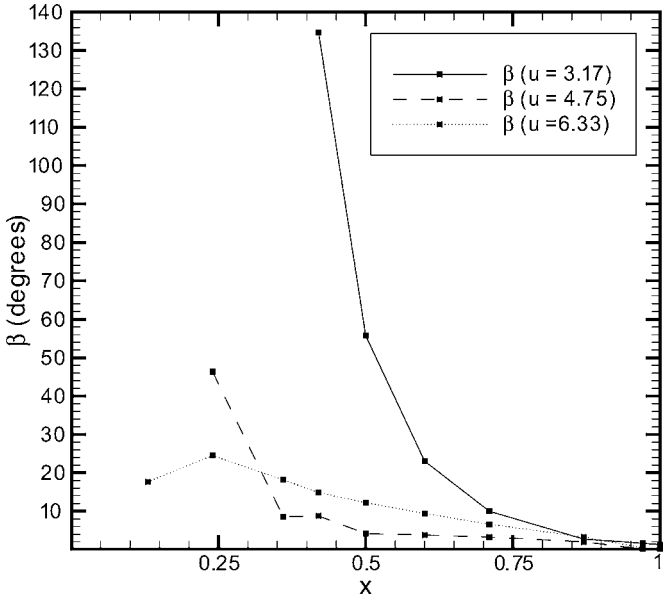

FIG. 25. Average deflection β of clusters C^A and C^B against the impact factor, x, for collision dynamics in mode (II).

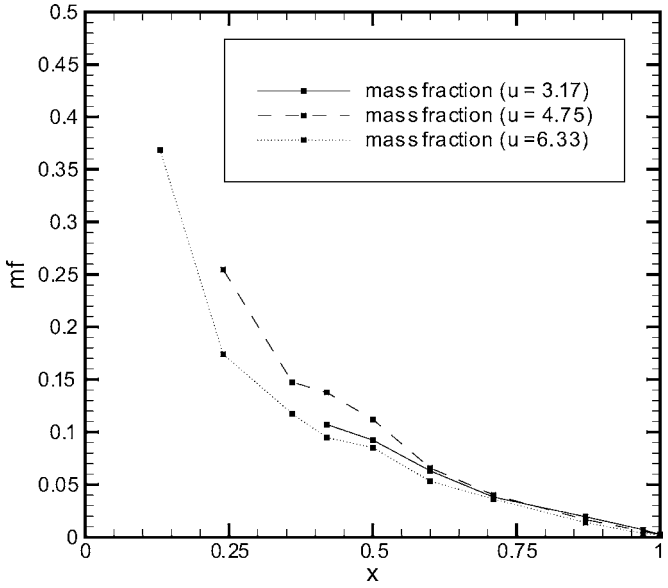

FIG. 26. Average mass fraction mf against the impact factor x for collision dynamics in mode (II).

ration occurs for high impact factors and/or at high velocities (see Fig. 5), and can be further classified into three submodes: (a) *normal stretching separation*, (b) *stretching separation with satellite droplets*, and (c) *shearing off*.

A collision is considered to belong to submode (b) if there is at least one large fragment beside the two main fragments, while the submodes (a) and (c) can be distinguished only by observation.

1. Normal stretching separation (IIa)

Collision dynamics in normal stretching separation share similarities with the slide-and-locking coalescence mode (Fig. 6). The major difference is that for the normal stretching separation the sliding motion is so distinct that stretching of the temporarily formed cluster causes separation again. Below we explain the collision dynamics for a typical case corresponding to $x=0.42$ and $u=3.17$ (Fig. 20). The first part of the collision is identical to that in slide-and-locking mode. Following the impact both clusters are flattened along the interface plane and start to slide along each other. In contrast to mode (Ib) the sliding motion lasts longer because of higher velocity u and/or smaller contact interface due to higher x. As the sliding continues the distance between the original clusters increases. This leads to a narrower contact interface and reduced binding forces. Eventually, the contact interface shrinks until it breaks. At this point the temporary common fragment has turned around 135 degrees before splitting into two clusters again. The centrifugal forces prevail over the binding forces, whereas in mode (Ib) the situation is reversed. Figure 20 shows that from $t=23.2$ onwards the interface starts to contract until it becomes very thin at $t=115.2$ and eventually breaks apart.

The trajectories of the original clusters C^A and C^B, as well as the distance $r^{A,B}$, are plotted in Figs. 21 and 22, respectively. The trajectories indicate sliding after the first contact of the clusters. The clusters enter a circular path and the distance $r^{A,B}$ increases linearly (or almost linearly) for all cases in collision mode (II). Note that there is no discontinuity at the separation point.

The conversion of the initial translational energy $E_{kl,\mathrm{ext}}$ is identical to mode (Ib). The only difference is that during stretching and separation the angular energy of the temporary aggregate is transformed back into translational energy $E_{kl,\mathrm{ext}}$ of the two final main fragments.

2. Stretching separation with satellite droplets (IIb)

For high velocities ($u>3.93$) and for a broad range of moderate impact factors ($0.13\leqslant x\leqslant 0.7$) the collisions belong to stretching separation mode including production of satellite droplets (Fig. 6). A satellite droplet is a large fragment which is not, however, one of the main fragments. Figure 23 shows the development of the collision for $x=0.42$ and $u=4.75$. Note that the impact parameter is the same as for mode (IIa), but at higher impact velocity. Similar to mode (IIa) the collision begins with flattening of the colliding clusters along a contact interface. Because of the higher initial impact energy, in the present case the process features scattering and faster stretching motion. Therefore, less rotation of the temporary common fragment occurs for (IIb) compared to (IIa).

The material at the contact interface is stretched into a long tubular mass. Around $t=69$ one can observe the formation of three necks along the stretched connection. These are the points in which the connection breaks into two satellite droplets, while the two main fragments still continue to move straight into opposite directions (see Fig. 23 for $t=92.6$ and $t=115.6$).

The trajectories of the main fragments are shown in Fig. 21 (dashed lines). After a short sliding the main fragments continue to travel along a straight line and, therefore, the distance $r^{A,B}$ increases linearly in time (Fig. 22).

3. Shearing-off (IIc)

For $x>0.8$ the overlapping cross section of the original clusters (see Sec. IV) becomes very small, thus the collision is minimized and the internal structure of the original clusters is not significantly altered. This case is referred to as shearing-off mode and a typical scenario is demonstrated in Fig. 24 for $x=0.87$ and $u=6.33$. The trajectories are shown in Fig. 21 and the distance of the mass centers in Fig. 22. The binding forces of the material in the collision region are too small to withstand the inertia of the entire cluster, thus fragments of the material are sheared off. The collision also results in slight rotation of both clusters. In the shearing-off mode a small percentage of $E_{kl,\mathrm{ext}}$ is converted into potential energy, $E_{p,\mathrm{int}}$, and kinetic energy, E_k, of the scattered atoms.

4. Effects of the impact factor on stretching separation mode

To assess the effects of the impact factor, x, on the clusters' deflection and molecular mixing, we have employed two parameters: (i) the deflection, β, of a cluster, which is defined by the angle between the initial velocity vector, $\boldsymbol{u}$, and the velocity vector of the cluster after the collision; and (ii) the mixing parameter, mf, representing the mass fraction of a main fragment that consists of atoms from the other cluster.

The difference of β^A and β^B was insignificant for all cases: less than 5% for high u in connection with low x, otherwise less than 1%. Figure 25 shows the average of β^A and β^B against different impact factor values. As expected, β tends to zero when $x\rightarrow 1$. For $u=3.17$, β increases exponentially when decreasing x; lower x entails higher overlapping regions leading to stronger interaction with the highest value measured in the borderline to coalescence (for $x=0.5$), where the common cluster rotates 135 degrees before it separates.

The mf values for the two main fragments differ less than 6% for low x combined with high u and less than 1% in all other cases. Figure 26 shows the averaged mass fraction mf against x. The three curves for the velocities almost coincide, suggesting that the impact velocity has no influence. Instead, the mixing depends primarily on the impact factor and increases faster for smaller x, reaching a peak value of mf=0.36 for $x=0.13$.

VI. DISCUSSION AND RELATION TO MACROSCOPIC DROPLET COLLISIONS

In the past, collisions of droplets at macroscopic scales have been the subject of many experimental[1,2,11,12,15] and numerical[17,18] investigations. The setup of these experiments is very similar to the present simulations. There are, however, two noticeable differences. First, the length scale of the present simulations is smaller by five orders of magnitude than the macroscopic droplet experiments. Second, in the macroscopic case the droplets are in liquid phase and retain the same temperature throughout the simulation. At nanoscale the temperature of the clusters varies significantly during the development of the collision: the clusters are initially in a solid phase and depending on the collision scenario they are transformed to liquid droplets. Similar to previous studies,[23–26] we examine below similarities in the collision dynamics of droplets at macroscale and nanoscale, despite the mentioned differences.

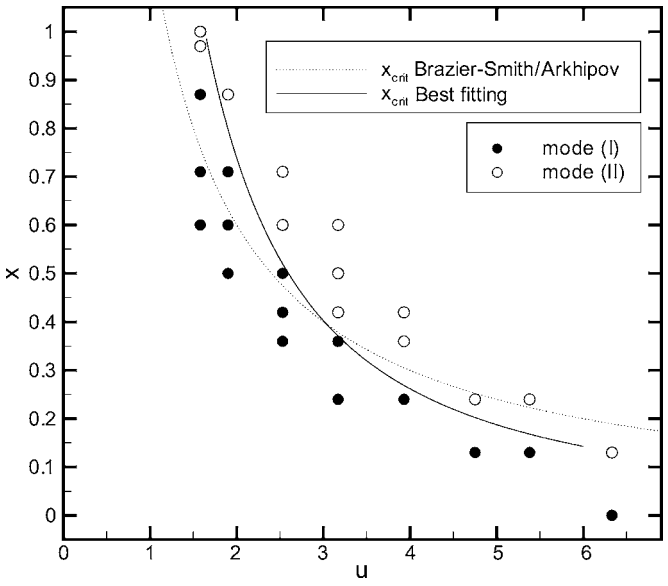

FIG. 27. Comparison of the macroscopic analytical model (dashed line) of Brazier-Smith *et al.* (Ref. 11) [Eq. (8)] with the present MD simulation results as well as an alternative model $x_{\mathrm{crit}}=au^b$, $a=2$, and $b=-1.5$ (solid line) proposed here.

Binary droplet collisions at macroscales are characterized by the impact factor x and the Weber number, We $=(\rho d/\gamma)u^2$, where ρ is the density and γ is the surface tension. Four modes have been observed: coalescence, stretching separation, reflexive separation, and shattering. These modes correspond to the ones described in the preceding section for collisions at nanoscale. The reflexive separation mode is observed at macroscales for almost central collisions ($x<0.25$) at high velocities (We$\geqslant$19).[1] Here, the two droplets merge to a temporary common droplet, which is elastically flattened into a disclike or a toruslike shape during impact. The subsequent reflexive motion, caused by surface tension, reshapes the formed droplet into an elongated cylinder that eventually breaks up into two droplets. Depending on the values of the Weber number and impact factor satellite droplets may be formed.

For the length scales less than 10^{-8} m considered here, reflexive separation was not observed. This agrees with previous studies for clusters smaller than the ones considered here, e.g., LJ_{1000},[25] $(\mathrm{H2O})_{729}$,[24] and $(\mathrm{H2O})_{1000}$.[26] We note that the clusters in the present study are initially in solid state and, therefore, one cannot exclude the possibility that reflexive separation may occur for liquids at nanoscale. Because the clusters are immediately liquified one could argue that the initially solid state is not the reason for the absence of

reflexive separation. Nevertheless, this is a subject of a separate investigation.

Because all macroscopic investigations have been carried out using liquid droplets, submodes associated with the coalescence mode have not been previously reported.[1] Comparison with the results of Brenn *et al.*[12] shows that the formation of satellite droplets in the stretching separation mode can be much more pronounced at macroscales than at nanoscales.

Previous investigations of macroscopic binary droplet collisions have pursued to find analytical criteria that describe the boundaries between coalescence and stretching separation.[1,11,15] Ming *et al.*[25] found satisfactory accuracy between MD simulation results for binary collisions of Ar_{1000} clusters and the analytical model predictions of Brazier-Smith *et al.*[11] The Brazier-Smith model is based on the balance of centrifugal forces and forces originating from the surface tension. For droplets of the same diameter, d, the transition criterion is given by

$$x_{\mathrm{crit}} = \left(c \sqrt{\frac{\gamma}{\rho d}} \right) \frac{1}{u}, \tag{8}$$

where different values of the constant c have been proposed: $c=2.50$ by Brazier-Smith *et al.*[11] and $c=3.47$ by Arkhipov *et al.*[15] In the present paper the density ρ of the initial cluster is $1.042\ m_a/\sigma^3$. In general, it is difficult to estimate the surface tension γ of Lennard-Jones clusters[46] since this depends on the internal structure and temperature of the clusters,[47] which, however, changes during the collision process.

When using the same surface tension value as Ming *et al.*,[25] i.e., $\gamma=1.7\epsilon/\sigma^2$, we obtain similar predictions from the analytical model and simulations. However, the best agreement between the Brazier-Smith-Arkhipov model and the present results is obtained for $c\sqrt{\rho d/\gamma}=1.2$ (Fig. 27). For the d and ρ considered here, the value of $c\sqrt{\rho d/\gamma}=1.2$ implies a surface tension γ in the range of $3.4-6.5\epsilon/\sigma^2$. These values are still within the range of the surface tension for Lennard-Jones clusters.[48]

The discrepancies between the analytical models and simulations may be due to the following reasons.

For macroscopic particles, the temperature varies insignificantly compared to the nanoparticle case: the smaller the particle size the higher the temperature rise during the collision. Let us consider two pairs of particles a and b with diameters d_a and d_b, respectively, and a diameter ratio f, $d_b=d_a f$. For identical Weber numbers $u_b^2=u_a^2/f$ thereby for smaller particles the impact velocity is higher. Using the definition of the Weber number, we obtain

$$u_b^2 = \frac{\mathrm{We}\ \gamma}{\rho d_a f}. \tag{9}$$

For central impact ($X=0$), the external kinetic energy, $E_{k\ \mathrm{ext}}=\frac{1}{2}mu^2$, is converted entirely into internal energy. The temperature then changes as

$$\Delta T_b = \frac{E_{k\ \mathrm{ext}\ b}}{2cm} = \frac{mu_b^2}{4cm} = \frac{u_b^2}{4c} = \frac{\mathrm{We}\ \gamma}{4c\rho d_a f}, \tag{10}$$

with c being the specific heat capacity, where u_b^2 has been replaced by (9). According to (10), $\Delta T_b \sim 1/f$, i.e., the smaller the particles the higher the temperature rise (for binary collisions of comparable outcome).

As an example, we compare the temperature rise for water droplets of diameter 500 μm, such as in the Ashgriz[1] experiments, with that of water particles of diameter 10 nm as used in the presented study. For a typical Weber number We=35; density of water $\rho=1003\ \mathrm{kg/m^3}$; surface tension $\gamma=73\times10^{-3}$ N/m; and specific heat capacity $c_p=4.187$ J/gK, the droplets of 500 μm colliding with a velocity of 2.26 m/s result in a temperature rise of 3×10^{-4} K. This temperature rise should not influence material properties such as surface tension and viscosity. However, for the nanoscale particles with $d=10$ nm a collision with the same characteristics at 505 m/s will result in a temperature rise of 15 K. Monoatomic substances like the ones used in the present study have lower heat capacity and, therefore, the temperature rise will be even higher. For the cases considered in the present paper, We=35 and $X=0$, the temperature rise was about 30 K (considering that the LJ-potential represents argon cluster).

For the nanoparticles considered here phase transformation occurs, with the temperature and phase of the material influencing the strength of the binding forces and, hence, the details of the collision dynamics including the transition regime.

Finally, scattering of atoms, especially at high impact velocities, reduces the size of the clusters in some cases significantly. This effect is not observed in macroscopic droplets and it is not, therefore, accounted for by (8). A better fit of the simulation data can be obtained by using $x_{\mathrm{crit}}=au^b$ instead of (8), with $a=2$ and $b=-1.5$ for best fitting. This result is plotted as a solid line in Fig. 27.

VII. SUMMARY OF CONCLUSIONS

Molecular dynamics models offer the possibility to investigate the details of nanoparticle (molecular clusters or droplets) collisions, which are more difficult to be studied by experiments due to the small length and time scales involved. We have investigated the collision dynamics of nanoclusters for a broad range of impact factors and speeds. Similar to macroscopic droplet collisions, coalescence and stretching were also found in the present case. Reflexive separation, another mode observed in macroscopic droplet collisions, was not found for the collision of the initially solid nanoclusters.

Detailed analysis of the collision processes has revealed different submodes that lead to coalescence, which are classified according to their dynamics into sticking (Ia), slide-and-locking (Ib), and droplet (Ic) modes. Submodes also exist within stretching separation: normal stretching separation (IIa), stretching separation with satellite droplets (IIb), and shearing off (IIc). Macroscopic analytical models that describe the borderline between coalescence and stretching

separation were found to describe qualitatively the transition between the two modes at nanoscale. The development of a new analytical model that describes collision mode boundaries at nanoscale requires further understanding of the transition between modes (Ib) and (II). This requires simulations for larger clusters and droplets to be conducted in order to find the lower length-scale limit for the occurrence of reflexive separation. Future studies should also include a vapor atmosphere surrounding the cluster in order to capture the equilibrium between evaporation and condensation.

*Electronic address: m.kalweit@cranfield.ac.uk
†Electronic address: d.drikakis@cranfield.ac.uk

[1] N. Ashgriz and J. Y. Poo, J. Fluid Mech. **221**, 183 (1990).
[2] J. Qian and C. K. Law, J. Fluid Mech. **331**, 59 (1997).
[3] S. L. Post and J. Abraham, Int. J. Multiphase Flow **28**, 997 (2002).
[4] G. H. Ko and H. S. Ryou, J. Aerosol Sci. **36**, 1300 (2004).
[5] R. C. Flagan and M. M. Lunden, Mater. Sci. Eng., A **204**, 113 (1995).
[6] R. Zachariah and M. J. Carrier, J. Aerosol Sci. **30**, 1139 (1999).
[7] R. L. Johnston, *Atomic and Molecular Cluster* (Taylor and Francis, London, 2002).
[8] J. M. Soler, N. García, O. Echt, K. Sattler, and E. Recknagel, Phys. Rev. Lett. **49**, 1857 (1982).
[9] J. Eggers, J. Lister, and H. Stone, J. Fluid Mech. **401**, 293 (1999).
[10] H. Stone, Annu. Rev. Fluid Mech. **26**, 65 (1994).
[11] P. R. Brazier-Smith, S. G. Jennings, and J. Latham, Proc. R. Soc. London, Ser. A **326**, 393 (1972).
[12] G. Brenn, D. Valkovska, and K. D. Danov, Phys. Fluids **13**, 2463 (2001).
[13] K. D. Willis and M. E. Orme, Exp. Fluids **29**, 347 (2001).
[14] K. D. Willis and M. E. Orme, Exp. Fluids **34**, 28 (2003).
[15] V. A. Arkhipov, I. M. Vasenin, and V. F. Trofimov, Prikl. Mekh. Tekh. Fiz. **3**, 95 (1983) [J. Appl. Mech. Tech. Phys. **24**, 371 (1983)].
[16] A. Gopinath and R. L. Koch, J. Fluid Mech. **454**, 145 (2002).
[17] M. Rieber and A. Frohn, J. Aerosol Sci. **26**, 929 (1995).
[18] M. Schelke and A. Frohn, J. Aerosol Sci. **26**, 145 (1995).
[19] F. Mashayek, N. Ashgriz, W. J. Minkowycz, and B. Shotorban, Int. J. Heat Mass Transfer **46**, 77 (2003).
[20] Y. Meleán and L. D. G. Sigalotti, Int. J. Heat Mass Transfer **48**, 4041 (2005).
[21] Y. Pan and K. Suga, Phys. Fluids **17**, 082105 (2005).
[22] D. Greenspan, Comput. Math. Appl. **19**, 91 (1990).
[23] D. Greenspan and F. L. Heath, J. Phys. D **24**, 2121 (1991).
[24] B. Wyatt, Comput. Math. Appl. **28**, 175 (1994).
[25] L. Ming, N. Markovic, M. Svanberg, and J. B. C. Petterson, J. Phys. Chem. A **101**, 4011 (1997).
[26] M. Svanberg, L. Ming, N. Markovic, and J. B. C. Pettersson, J. Chem. Phys. **108**, 5888 (1998).
[27] M. Kalweit and D. Drikakis, J. Comput. Theor. Nanosci. **1**, 367 (2004).
[28] E. Blaisten-Barojas and M. R. Zachariah, Phys. Rev. B **45**, 4403 (1992).
[29] R. Schmidt, G. Seifert, and H. Lutz, Phys. Lett. A **158**, 231 (1991).
[30] T. Hawa and M. R. Zachariah, Phys. Rev. B **69**, 035417 (2004).
[31] T. Hawa and M. R. Zachariah, Phys. Rev. B **71**, 165434 (2005).
[32] T. Hawa and M. R. Zachariah, J. Aerosol Sci. **37**, 1 (2006).
[33] J. Rogan, Ramirez, A. H. Romero, and M. Kiwi, Eur. Phys. J. D **28**, 219 (2003).
[34] S. Arcidiacono, N. R. Bieri, D. Poulikakos, and C. P. Grigoropoulos, Int. J. Multiphase Flow **30**, 979 (2004).
[35] M. P. Allen and D. J. Tildesley, *Computer Simulation of Liquids* (Oxford University Press, Oxford, England, 1987).
[36] K. Bolton, M. Svanberg, and J. B. C. Petterson, J. Chem. Phys. **110**, 5380 (1999).
[37] M. Moseler, Nucl. Instrum. Methods Phys. Res. B **164**, 522 (2000).
[38] Y. Yamaguchi and J. Gspann, Phys. Rev. B **66**, 155408 (2002).
[39] A. Tomsic, H. Schröder, K.-L. Kompa, and C. R. Gebhardt, J. Chem. Phys. **119**, 6314 (2003).
[40] S. Prasalovich, Ph.D. thesis, Department of Experimental Physics, Göteborg University, 2003.
[41] D. Drikakis and M. Kalweit, in *Handbook of Computational Nanotechnology* (American Scientific, New York, 2006).
[42] K. Refson, Comput. Phys. Commun. **126**, 309 (2000).
[43] S. D. Stoddard, Comput. Chem. (Oxford) **27**, 291 (1978).
[44] H. Goldstein, C. Poole, and J. Safko, *Classical Mechanics* (Addison-Wesley, San Francisco, 2002).
[45] W. Humphrey, A. Dalke, and K. Schulten, J. Mol. Graphics **14**, 33 (1996).
[46] Q. Sun and D. B. Iain, in *38th AIAA Thermophysics Conference 6–9 June 2005* (AIAA, Toronto, Canada, 2005), pp. AIAA-2005–4831.
[47] S. Sinha, V. K. Dhir, and B. Shi, in *2003 ASME Summer Heat Tranfer Conference July 21–28,2003, Las Vegas, Nevada USA* (ASME, Las Vegas, 2003), pp. HT2003–47164.
[48] T. Ikeshoji, G. Torchet, and K. Koga, Eur. Phys. J. D **24**, 211 (2003).